Inorganic Chemistry
Article
pubs.acs.org/IC

Lattice-Matched Transition Metal Disulfide Intergrowths: The Metallic Conductors $Ag_2Te(MS_2)_3$ (M = V, Nb)

Sandy L. Nguyen,[†] Christos D. Malliakas,[†] Melanie C. Francisco,[†] and Mercouri G. Kanatzidis*[,†,‡]

[†]Department of Chemistry, Northwestern University, Evanston, Illinois 60208, United States
[‡]Materials Science Division, Argonne National Laboratory, Argonne, Illinois 60439, United States

S *Supporting Information*

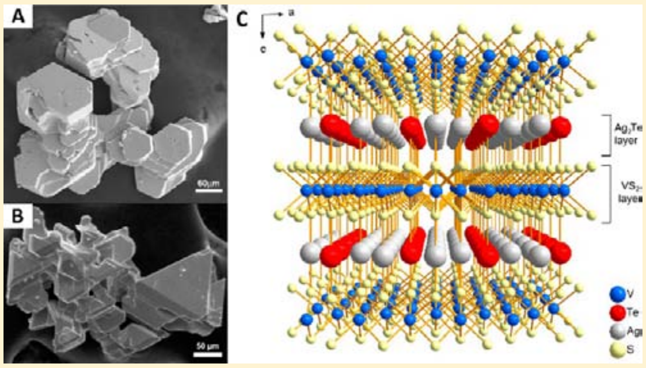

ABSTRACT: We present new chalcogenide compounds, $Ag_2Te(MS_2)_3$ (M = V, Nb), built up of alternating planes of $[MS_2]$ and $[Ag_2Te]$. The Ag and Te atoms are linearly coordinated by S atoms in the $[MS_2]$ layers and held in place by covalent interactions. Structural polymorphism was found by single crystal X-ray diffraction studies, where long-range ordering or disorder of the Ag and Te atoms within the hexagonal planar $[Ag_2Te]$ layer yielded two distinct crystal forms. When the Ag and Te atoms are ordered, the two isostructural compounds crystallize in the non-centrosymmetric $P\bar{6}2m$ space group, with $a = 5.5347(8)$ Å, $c = 8.0248(16)$ Å, and $V = 212.89(6)$ Å^3 for α-$Ag_2Te(VS_2)_3$ and $a = 5.7195(8)$ Å, $c = 8.2230(16)$ Å, and $V = 232.96(6)$ Å^3 for α-$Ag_2Te(NbS_2)_3$. For the occupationally disordered Ag/Te arrangement, a subcell of the ordered phase that crystallizes in the non-centrosymmetric $P\bar{6}m2$ space group, with $a = 3.2956(6)$ Å $(=a_a/(3)^{1/2})$, $c = 8.220(2)$ Å, and $V = 77.31(3)$ Å^3 for β-$Ag_2Te(VS_2)_3$, was identified. Furthermore, pair distribution function analysis revealed local distortions in the $[Ag_2Te]$ layer. Band structure calculations at the density functional theory level were carried out to investigate the electronic structure of $Ag_2Te(MS_2)_3$. Electronic transport measurements on $Ag_2Te(MS_2)_3$ show that they exhibit p-type metallic behavior. Thermal analyses and temperature-dependent powder X-ray diffraction studies were focused on the stability and transformation/decomposition of the $Ag_2Te(MS_2)_3$ phases. Magnetic susceptibility data are also reported. The new intercalated $Ag_2Te(MS_2)_3$ system features a unique hypervalent Te with a three-center, four-electron bonding environment isoelectronic to that found in I_3^-.

■ INTRODUCTION

Layered transition metal dichalcogenides (TMDCs) have been shown to possess interesting anisotropic electronic, magnetic, structural, and mechanical properties.[1] The TMDCs range from semiconductors and insulators, in the case of group 4, 6, and 14 dichalcogenides, to metallic compounds, in the case of group 5 TMDCs. Group 5 TMDCs have also been found to exhibit Pauli paramagnetism, superconductivity,[1,2] and charge density waves.[2a] These anisotropic properties result from the two-dimensional, hexagonal structures of the TMDCs; the transition metal (M) is either found in an octahedral or a trigonal prismatic coordination by chalcogen (Q) atoms in a $Q-M-Q$ sandwich-like arrangement. While a wide range of polytypes are possible, TMDCs with the metal atoms in d^0, d^1, or d^2 configurations tend to be stabilized in the trigonal prismatic coordination, known as the 2H polytype.[3] Within the category of group V disulfides, VS_2 has only been synthesized in the so-called 1T form (octahedral coordination of the V atom),[4] while NbS_2 and TaS_2 can be found in a wide range of polytypes.[1] In addition, superconducting transition temperatures (T_c) can vary by polytype, with 2H-NbS_2 and 2H-TaS_2 showing T_c values of 6.3[5] and 0.8 K,[6] respectively.

The $Q-M-Q$ layers are held together by weak van der Waals interactions which allow for intercalation by metal atoms or organic molecules,[7] potentially altering the electronic and magnetic properties relative to the pure TMDCs.[8] In trigonal prismatically coordinated group V TMDCs with the formula MQ_2 (M = Nb, Ta; Q = S, Se), it has been suggested that intercalation results in electron transfer to the partially unoccupied "d_{z^2}" band, which is half-filled and only contains one electron.[3,8,9] In TMDCs with metal intercalants, the guest atoms can be in tetrahedral, octahedral, trigonal prismatic, or linear coordination environments within the van der Waals gap of the parent lattice.[7a,10] So-called misfit compounds have also been reported, which feature the parent TMDC structure intercalated with binary compounds possessing 2D square lattices that are incommensurate with the parent structure. For example, $(SnS)_{1.18}NbS_2$ has been shown to feature a square SnS lattice intercalated between the hexagonal parent NbS_2 layers.[11]

Here, we report two new transition metal dichalcogenide derivative compounds, $Ag_2Te(MS_2)_3$ (M = V, Nb), featuring the respective disulfide framework compounds, VS_2 and NbS_2,

Received: February 24, 2013
Published: May 14, 2013

intercalated with planar Ag_2Te. The intercalant Ag and Te atoms are bonded to the MS_2 layers via Ag−S and Te−S interactions, forming linear fragments of S−Ag−S and S−Te−S, respectively. Adding to the structural novelty of these compounds is the fact that the pure parent dichalcogenide VS_2 has only been synthesized in the 1T polytype (octahedral coordination of the V atom). Trigonal prismatic VS_2 has only been reported in the intercalated $AuVS_2$, a compound structurally related to the $Ag_2Te(MS_2)_3$ compounds reported here. $Ag_2Te(VS_2)_3$ was discovered via low temperature (350 °C) alkali metal mixed-polychalcogenide flux reactions and contains both S and Te in different crystallographic sites and oxidation states. $Ag_2Te(NbS_2)_3$, the Nb-containing structural analogue, was discovered thereafter by direct combination of the elements.

Band structure calculations at the density functional theory (DFT) level were carried out to compare the electronic structures of $Ag_2Te(MS_2)_3$ to those of the parent MS_2 compounds, and electronic transport measurements on $Ag_2Te(MS_2)_3$ show that they exhibit p-type metallic behavior. Temperature-dependent powder X-ray diffraction studies were performed to assess the stability and transformation/decomposition of the $Ag_2Te(MS_2)_3$ phases. Magnetic properties measurements performed on the reported compounds show weak paramagnetic behavior, with an antiferromagnetic transition in $Ag_2Te(VS_2)_3$ at 30 K.

Structural determination using single crystal and selected area electron diffraction was performed on the crystals, and a structural polymorphism was observed depending on the occupational ordering of Ag and Te atoms in the $[Ag_2Te]$ layer. Specifically, the ordered structure, α-$Ag_2Te(MS_2)_3$, forms a $(3)^{1/2}a \times (3)^{1/2}b$ supercell with respect to the MS_2 subcell, β-$Ag_2Te(MS_2)_3$. Pair distribution function (PDF) analysis revealed local distortions in the $[Ag_2Te]$ layer, indicating that weak covalent interactions within the layers act to stabilize the unique linear coordination of the intercalant atoms. X-ray absorption near edge spectroscopy (XANES) studies imply that the composite layered structure of the $Ag_2Te(MS_2)_3$ compounds is held together by a very small degree of charge transfer between the layers. Our results suggest that the intercalant Te atoms remain close to a Te^0 oxidation state, such that the unique linear $[S{-}Te{-}S]^{4-}$ moiety found in $Ag_2Te(MS_2)_3$ is a three-center, four-electron bond that is isoelectronic to the linear species I_3^-. Moreover, the hexagonal arrangement of atoms in the Ag_2Te layer is unprecedented for silver telluride. The intergrowth $(Ag_2Te)(MS_2)$ compounds contribute a new type of intercalation motif to the well-studied class of TMDCs and suggest the possibility of other metastable arrangements of guest species stabilized between host MS_2 layers.

EXPERIMENTAL SECTION

Materials. The following reagents were used as obtained from the manufacturer: (i) Rubidium metal, analytical reagent, Aldrich Chemical Co., Milwaukee, WI. (ii) Sulfur powder, sublimed; vanadium metal, analytical reagent; niobium metal, analytical reagent, J. T. Baker Chemical Co., Phillipsburg, NJ. (iii) Silver powder, Fisher Scientific Co., FairLawn, NJ. (iv) Tellurium powder 99.999%, Atlantic Metals Atlantic Metals & Alloys, LLC., Stratford, CT. (v) *N*,*N*-Dimethylformamide (DMF), analytical reagent; diethyl ether, anhydrous; carbon disulfide, Mallinckrodt Baker, Inc., Phillipsburg, NJ.

Syntheses. Alkali metal chalcogenide Rb_2S was synthesized in liquid ammonia from Rb metal and sulfur according to a modified literature procedure.[12] All manipulations were performed in a glovebox under inert nitrogen atmosphere. All reactions were run in a computer controlled furnace. Each flux reaction mixture was repetitively washed with degassed DMF under N_2 atmosphere until the flux was completely removed. The flux reaction product was finally obtained after further washing with diethyl ether, and dried in air. Direct reaction products were washed with carbon disulfide to remove excess sulfur. Heating of $Ag_2Te(VS_2)_3$ up to 780 °C with one end of the tube exposed outside of the furnace resulted in deintercalation of the product into binary materials (V_3S_4, V_5S_8, and Ag_2Te).[13] However, reformation of the $Ag_2Te(VS_2)_3$ single phase was performed successfully with an extended hold (1−2 weeks) and excess S at 550 °C.

Preparation of $Ag_2Te(VS_2)_3$. Amounts of 0.102 g (0.5 mmol) of Rb, 0.027 g (0.25 mmol) of Ag, 0.032 g (0.25 mmol) of Te, 0.013 g (0.25 mmol) of V, and 0.064 (2.0 mmol) of S were mixed and loaded into a fused silica tube. The tube was evacuated to 10^{-3} Torr and flame-sealed. It was then held at 350 °C for 5 days, followed by cooling to 50 °C over 75 h. Extraction in DMF yielded a product of very fine, light pink metallic crystalline powder. Subsequent attempts to resynthesize this compound via flux synthesis yielded varied results, with either crystalline powder and unwanted secondary product ($RbAgTeS_3$)[14] or an alternate phase altogether (Rb_2AgVS_4).[15] The presence of Ag, Te, V, and S in single crystals and powder samples was confirmed using semiquantitative energy dispersive X-ray (EDX) analysis on a Hitachi S-3400 scanning electron microscope (SEM) with a PGT energy dispersive X-ray analyzer. An average composition of $Ag_{1.9}Te_1V_{2.9}S_{5.9}$ was found from EDX/SEM analysis on a large number of single crystals.

Alternate Preparation of $Ag_2Te(VS_2)_3$. Amounts of 0.054 g (0.5 mmol) of Ag, 0.032 g (0.25 mmol) of Te, 0.039 g (0.75 mmol) of V, and 0.056 g (1.75 mmol) of S were mixed and loaded into a fused silica tube. The tube was evacuated to 10^{-3} Torr and flame-sealed. It was then heated to 600 °C in 12 h, held at 600 °C for 6 h, heated to 800 °C in 6 h, and held at 800 °C for 6 days, followed by cooling to 50 °C over 2 days. Extraction from the tube yielded a product of light pink metallic crystals. The products were further purified by placing one end of the tube into a furnace set at 500 °C and leaving the other end of the tube out of the furnace for 24 h to condense any excess sulfur at the cold end of the tube.

Preparation of $Ag_2Te(NbS_2)_3$. Amounts of 0.054 g (0.5 mmol) of Ag, 0.032 g (0.25 mmol) of Te, 0.070 g (0.75 mmol) of Nb, and 0.056 g (1.75 mmol) of S were mixed and loaded into a fused silica tube. The tube was evacuated to 10^{-3} Torr and flame-sealed. It was then heated to 600 °C in 12 h, held at 600 °C for 6 h, heated to 800 °C in 6 h, and held at 800 °C for 6 days, followed by cooling to 50 °C over 2 days. Extraction from the tube yielded a homogeneous product of crystals with a metallic luster. An average composition of $Ag_{2.0}Te_1Nb_{3.0}S_{5.9}$ was found from EDX/SEM analysis on a large number of single crystals.

X-ray Diffraction Studies. Powder X-ray diffraction (XRD) was performed at room temperature on both compounds for identification and analysis of phase purity. XRD data were recorded on a NIST (National Institute of Standards and Technology) Si-calibrated Inel CPS 120 diffractometer with a position-sensitive detector and graphite-monochromatized Cu Kα radiation operating at 40 kV and 20 mA.

Structure determination on single hexagonal crystals of α-$Ag_2Te(VS_2)_3$ and triangular crystals of α-$Ag_2Te(NbS_2)_3$ was performed at 293 and 100 K, respectively using a STOE image plate diffraction system (IPDS II) diffractometer with graphite-monochromatized Mo Kα radiation (λ = 0.71073). Data reduction and numerical absorption corrections were done using the STOE X-Area software.[16] Two data sets were collected for each crystal structure and merged using the scaling feature of X-Area to ensure completeness. The data sets were integrated and absorption corrections were performed separately before merging. Single-crystal X-ray diffraction data for the disordered β-$Ag_2Te(NbS_2)_3$ were collected with the use of MX optics-monochromatized Cu Kα radiation (λ = 0.154178 Å) on a Bruker SMART APEX CCD area detector diffractometer. Intensity data were collected by several ω and φ scans with a step of 0.5° and an exposure time of 15 s/frame with the program APEX2.[17] Cell refinement and data reduction were accomplished with the use of the program SAINT,[17] and a face-indexed absorption correction was performed numerically with the use of the program XPREP.[18] Then, the program SADABS[19] was employed to make incident beam and decay corrections. The structures were solved by direct methods and refined by full-matrix least-squares on F^2 (all data) using the SHELX software suite.[20]

High resolution *in situ* powder XRD measurements (30 keV, λ = 0.413 Å) of the samples above room temperature were performed at beamline BM-11-B at the Advanced Photon Source (APS) at Argonne National Laboratory (ANL). The samples were placed in quartz capillaries and spun as a hot gas blower was employed to bring sample temperatures up to 820 °C with steps of 5 °C/min. Measurements (3−5 min each) were taken continuously during the heating cycle.

Selected Area Electron Diffraction (SAED). All selected area electron diffraction experiments were carried out at room temperature on a Hitachi H8100 200 keV transmission electron microscope (TEM). Fujifilm image plates (BAS-IP SR 2040) with an active area of 80 mm × 95 mm were exposed for around 6 s with a camera length of 1 m and read with a Molecular Dynamics Storm 860 phosphoimager. A single crystalline platelet of each ordered α-$Ag_2Te(MS_2)_3$ member was glued on a copper aperture grid (Electron Microscopy Sciences) and ion-milled to the appropriate thickness with the aid of a Gatan Precision Ion Polishing System (691 PIPS).

Pair Distribution Function (PDF) Analysis. Pair distribution function analysis was performed on sieved samples (<50 μm) of $Ag_2Te(VS_2)_3$ and $Ag_2Te(NbS_2)_3$ packed in a Kapton capillary (1 mm diameter) and sealed with clay. The rapid acquisition pair distribution function (RA-PDF) technique[21] was used to collect diffraction data at room temperature using a Perkin-Elmer image plate detector and X-rays with an energy of 58 keV (λ = 0.2128 Å) at the 11-ID-B beamline at the APS at ANL. Counting statistics were improved by the collection of 200 frames per sample with an exposure time of 2 s per frame. The data were integrated using the program Fit2D,[22] and corrections (subtraction of background and container, Compton and fluorescence scattering, geometric and absorption corrections, etc.)[23] were performed using the program PDFgetX2.[24] The normalized data were truncated at 25 Å^{-1} before PDF calculation. PDFfit2 and PDFgui were used to simulate and model the data.[25]

X-ray Absorption Near Edge Spectroscopy (XANES). The oxidation states and local coordination environments of the metal atoms were analyzed by XANES at beamline BM-20-B of the APS. Vanadium (4563.76 eV)[26] K-edge, niobium (18982.97 eV)[26] K-edge, and tellurium (4341.4 eV)[27] L-edge XANES data were collected in transmission mode with gas ionization chambers to monitor the intensities of incident and transmitted X-rays. For V and Nb, the Si(111) double crystal monochromator was calibrated using V/Nb foil placed between the second and third ionization chambers for alignment of the edge positions. The first ionization chamber was filled with a He and N_2 gas mixture, and the second and third chambers contained N_2 gas. For Te, transmission data for a Te^0 reference was collected between each scan to validate monochromator stability. The monochromator step size was 0.20 eV (V, Te) or 1.0 eV (Nb) per step in the XANES region (5460−5540 eV for V, 4140−4440 eV for Te, and 18900−19100 eV for Nb). Energy calibrations were performed by assigning the maximum of the first derivative peak of the V or Nb foil or Te samples to the appropriate edge energies (E_0) mentioned above, respectively. Samples were prepared by thorough grinding, sieving to a particle size <15 μm, and carefully brushing a small amount of material on Kapton tape and folding it onto itself to minimize differences in thickness within the samples. The standards used were CuV_2S_4[28] for V (K-edge); $NaNbS_6$[29] and $NbSe_2$ for Nb (K-edge); and PbTe, Te, and $CsAgTeS_3$[14] for Te (L-edge). At least three scans were collected and averaged for each sample. XANES data were analyzed using Athena in the IFEFFIT software package.[30] The collected scans for each sample were checked for calibration, aligned, normalized, and averaged.

Charge Transport Measurements. Seebeck coefficient measurements were performed using a commercial MMR SB-100 Seebeck Measurement System under a vacuum between 305 and 700 K. Single crystal platelets were cut into rectangular shapes in arbitrary directions, and electrical contacts were applied using silver paste. The crystals were mounted in parallel with a constantan reference to monitor the temperature difference across the samples.

Four-probe high temperature electrical resistivity measurements were performed from room temperature to 700 K. Measurements were made for arbitrary current directions in the *ab* plane using standard four-point contact geometry. A homemade resistivity apparatus equipped with a Keithley 2182A nanovoltmeter, a Keithley 6220 Precision direct current (DC) source, and a high temperature vacuum chamber controlled by a K-20 MMR system was used. Data acquisition was controlled by custom-written software. A Quantum Design Physical Properties Measurement System (PPMS) was used to measure four-probe DC resistivity from 5 K to room temperature.

Magnetic Susceptibility. Magnetic susceptibilities were measured from 2 K to room temperature using a Quantum Design Magnetic Properties Measurement System (MPMS) SQUID magnetometer with a magnetic field strength of up to 10 kOe. Field-dependent magnetic susceptibilities were measured in gelatin capsules containing powdered samples (100−170 mg) at 2 K. Temperature-dependent magnetic measurements were then run on the same samples from 2 K to room temperature after or cooling in zero field or an applied field of 5−10 kOe. The experimental data were fitted against a modified Curie−Weiss law [$\chi = \chi_0 + C/(T - \theta)$], where χ is the molar magnetic susceptibility, χ_0 is the temperature-independent paramagnetic susceptibility, C is the Curie constant, and θ is the Curie temperature. μ_{eff} values are calculated using the equation $\mu_{\mathrm{mol}} = (8C)^{1/2}$, and normalized per V or Nb atom.

Band Structure Calculations. Electronic structure calculations were performed using the self-consistent full-potential linearized augmented plane wave method (LAPW)[31] within density functional theory (DFT),[32] using the generalized gradient approximation (GGA) of Perdew, Burke, and Ernzerhof[33] for the exchange and correlation potential. The values of the atomic radii were taken to be 2.3 au for Te, Ag, Nb, and V atoms and 2.1 au for S atoms, where au is the atomic unit (0.529 Å). Convergence of the self-consistent iterations was performed for 308 *k* points inside the irreducible Brillouin zone to within 0.0001 Ry with a cutoff of −6.0 Ry between the valence and core states. Scalar relativistic corrections were included and a spin−orbit interaction was incorporated using a second variational procedure.[34] The calculations were performed using the WIEN2k program.[35]

RESULTS AND DISCUSSION

The mixed polychalcogenide flux $Rb_2Te_xS_y$ was employed to produce new, mixed chalcogen compounds incorporating both Te and S in different crystallographic sites. The use of flux to obtain $Ag_2Te(VS_2)$ has once again demonstrated the power of this method for compound discovery. The $Ag_2Te(MS_2)_3$ compounds reported here are unique owing to the presence of a two-coordinate, linearly coordinated Te atom, which has only been reported in binary[36] or ternary[37] polytelluride compounds, with infinite linear Te chains or the five-membered Te_5^{4-} chain containing a linear Te_3^{4-} fragment in the middle. One more instance of linear Te coordination is seen in sterically hindered coordination species;[59] for example, in $\{(CH_3)_2Si[(t\text{-}C_4H_9)C_5H_3]_2Sc(PMe_3)\}_2(\mu\text{-}Te)\cdot C_6H_6$, where the Te atom is coordinated on both sides by Sc atoms.[38] No isolated triatomic Te_3^{4-} units have been found in the literature, although the triatomic Se_3^{4-} unit has been seen in the case of $Ba_2Ag_4Se_5$.[39] Linear Te coordination in the form of T-shaped or square planar complexes has been reported in organometallic complexes,[40] but the chemistry of these is not closely related to the compounds reported here. To our knowledge, the strictly two-coordinate, triatomic unit featuring linear coordination of Te solely by S atoms, found in $Ag_2Te(MS_2)_3$, has not been reported in the literature.

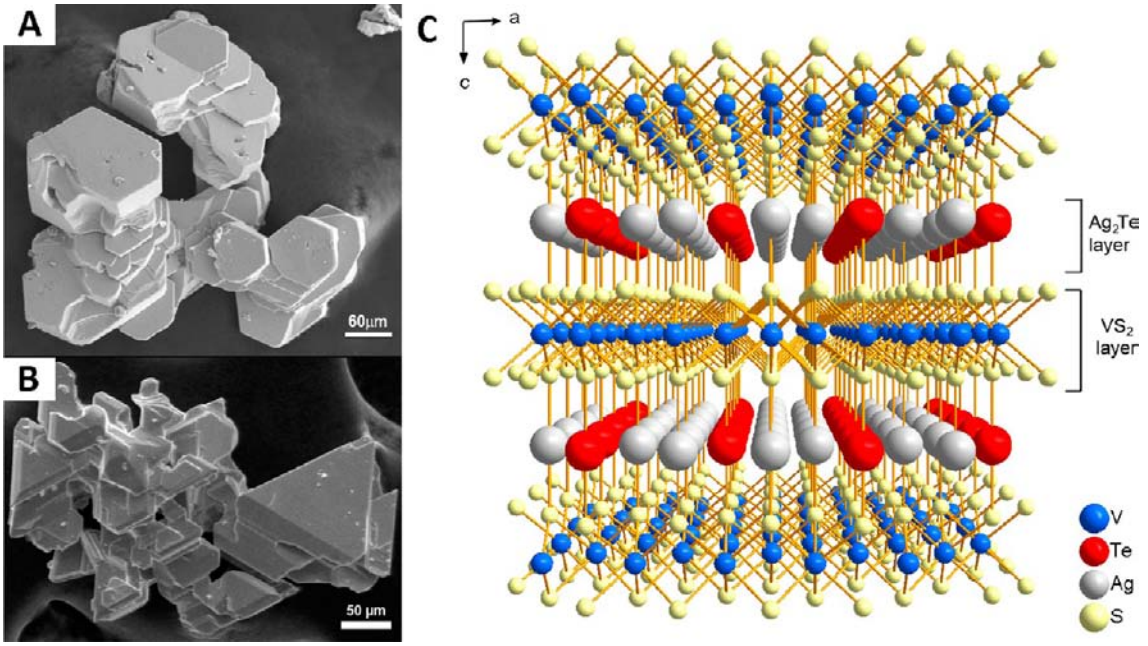

Figure 1. (A) SEM image of typical crystals of $Ag_2Te(VS_2)_3$; (B) SEM image of typical crystals of $Ag_2Te(NbS_2)_3$; (C) crystal structure of α-$Ag_2Te(VS_2)_3$ viewed along [010].

Table 1. Crystal Data and Structure Refinement for α-$Ag_2Te(VS_2)_3$, α- and β-$Ag_2Te(NbS_2)_3$, and $Ag_2Te(VS_2)_3$ in an *Amm*2 Orthorhombic Supercell[a]

compound	α-$Ag_2Te(VS_2)_3$	α-$Ag_2Te(NbS_2)_3$	β-$Ag_2Te(NbS_2)_3$	α'-$Ag_2Te(VS_2)_3$
formula weight	688.52	814.43	271.41	814.4
T (K)	293(2)	100(2)	100(2)	100(2)
crystal system	hexagonal	hexagonal	hexagonal	orthorhombic
space group	$P\bar{6}2m$	$P\bar{6}2m$	$P\bar{6}m2$	$Amm2$
a (Å)	5.5347(8)	5.7195(8)	3.2956(6)	8.8215(18)
b (Å)	5.5347(8)	5.7195(8)	3.2956(6)	9.903(2)
c (Å)	8.0248(16)	8.2230(16)	8.2190(19)	5.7190(11)
Z	1	1	1	2
V (Å^3)	212.98(6)	232.96(6)	77.31(3)	499.62(17)^3
ρ (g cm^{-3})	5.37	5.805	5.83	5.414
μ (mm^{-1})	12.435	12.046	98.929	11.233
F(000)	311	365	122	730
reflections collected	5027	4292	346	4030
unique data	461	392	73	971
R_{int}	0.0598	0.0911	0.0429	0.0697
parameters	16	20	8	43
R_1^a [$I > 2\sigma(I)$]	0.0478	0.0316	0.0374	0.0433
wR_2^b	0.0836	0.0868	0.0978	0.1250

[a] $R = \sum||F_o| - |F_c||/\sum|F_o|$, $wR = \{\sum[w(|F_o|^2 - |F_c|^2)^2]/\sum[w(|F_o|^4)]\}^{1/2}$, and calc $w = 1/[\sigma^2(F_o^2) + (aP)^2 + bP]$, where $P = (F_o^2 + 2F_c^2)/3$, and a and b are constants.

Crystal Structure Determination. Single crystal XRD was performed on hexagonal crystals of α-$Ag_2Te(VS_2)_3$ and triangular crystals of α-$Ag_2Te(NbS_2)_3$ (Figure 1). These compounds are isostructural and crystallize in the $P\bar{6}2m$ space group (Tables 1–5) with a = 5.5347(8) Å, c = 8.0248(2) Å, and V = 212.89(6) Å^3 for $Ag_2Te(VS_2)_3$ and a = 5.7195(8) Å, c = 8.2230(16) Å, and V = 232.96(6) Å^3 for $Ag_2Te(NbS_2)_3$. The compounds are composed of alternating planar layers of $[Ag_2Te]$ and $[MS_2]$ (Figure 2), more appropriately represented as α-$Ag_2Te(MS_2)_3$. These can be thought of as the parent disulfides with the sulfur atoms covalently bonded to the intercalant metal atoms (Ag and Te in a 2:1 ratio) in a linear coordination or, alternatively, intercalated by the two-dimensional planar hexagonal "Ag_2Te" lattice which is commensurate with the parent lattice. Like the binary NbS_2, the $[MS_2]$ layers in $Ag_2Te(MS_2)_3$ contain M in a trigonal prismatic coordination by the S atoms. These $[MS_2]$ layers are located directly above one another with no staggering of the layers, unlike other stacking polytypes seen in binary dichalcogenides (e.g., 2H-NbS_2, 2H-MoS_2, 3R-MoS_2).[1] The V–S and Nb–S bond lengths (~2.4 and ~2.5 Å, respectively) are similar to those of reported binary VS_2 and NbS_2 polytypes.

Detailed examination of the reciprocal lattice from X-ray diffraction on several α-$Ag_2Te(NbS_2)_3$ single crystals gave an unindexed fraction of around 3–5%. These reflections could not be indexed by the a_1 = 5.7087(8) Å and c_1 = 8.227(2) Å

Table 2. Atomic Coordinates ($\times 10^4$) and Equivalent Isotropic Displacement Parameters ($Å^2 \times 10^3$) for α-$Ag_2Te(VS_2)_3$ at 293(2) K with Estimated Standard Deviations in Parentheses

label	*x*	*y*	*z*	occupancy	U_{eq}[a]
Te	0	0	0	1	12(1)
Ag	3333	6667	0	1	46(1)
V	3409(3)	0	5000	1	7(1)
S(1)	6667	13333	3153(2)	1	8(1)
S(2)	0	0	3254(3)	1	8(1)

[a] U_{eq} is defined as one-third of the trace of the orthogonalized U_{ij} tensor.

Table 3. Anisotropic Displacement Parameters ($Å^2 \times 10^3$) for α-$Ag_2Te(VS_2)_3$ at 293(2) K with Estimated Standard Deviations in Parentheses[a]

label	U_{11}	U_{22}	U_{33}	U_{12}	U_{13}	U_{23}
Te	13(1)	13(1)	11(1)	6(1)	0	0
Ag	64(1)	64(1)	11(1)	32(1)	0	0
V	8(1)	6(1)	6(1)	3(1)	0	0
S(1)	8(1)	8(1)	7(1)	4(1)	0	0
S(2)	8(1)	8(1)	7(1)	4(1)	0	0

[a] The anisotropic displacement factor exponent takes the form $-2\pi^2[h^2a^{*2}U_{11} + ... + 2hka^*b^*U_{12}]$.

Table 4. Atomic Coordinates ($\times 10^4$) and Equivalent Isotropic Displacement Parameters ($Å^2 \times 10^3$) for α-$Ag_2Te(NbS_2)_3$ at 100(2) K with Estimated Standard Deviations in Parentheses[a]

label	*x*	*y*	*z*	occupancy	U_{eq}*
Te	0	0	0	1	6(1)
Ag	6600(30)	2780(20)	0	0.33	28(2)
Nb	3390(1)	0	5000	1	3(1)
S(1)	6667	3333	3070(2)	1	3(1)
S(2)	0	0	3160(2)	1	3(1)

[a] The anisotropic displacement factor exponent takes the form $-2\pi^2[h^2a^{*2}U_{11} + ... + 2hka^*b^*U_{12}]$.

Table 5. Anisotropic Displacement Parameters ($Å^2 \times 10^3$) for α-$Ag_2Te(NbS_2)_3$ at 100(2) K with Estimated Standard Deviations in Parentheses[a]

label	U_{11}	U_{22}	U_{33}	U_{12}	U_{13}	U_{23}
Te	6(1)	6(1)	4(1)	3(1)	0	0
Ag	53(3)	46(3)	9(1)	43(3)	0	0
Nb	3(1)	3(1)	4(1)	1(1)	0	0
S(1)	4(1)	4(1)	3(1)	2(1)	0	0
S(2)	3(1)	3(1)	3(1)	2(1)	0	0

[a] The anisotropic displacement factor exponent takes the form $-2\pi^2[h^2a^{*2}U_{11} + ... + 2hka^*b^*U_{12}]$.

hexagonal cell but with a smaller and related hexagonal cell with constants of a_2 = 3.2956(6) Å and c_2 = 8.219(2) Å at 100 K. While the longer *c*-axis is practically the same ($c_1 = c_2$) in both phases, the transformation relationship for the *a*- and *b*-axes is that of $a_1 = (3)^{1/2}a_2$. No apparent second phase in the form of a crystallite with a different habit or color was observed on the surface of the single crystals measured by X-rays, although minor domains (less than 5% in volume) of the same color and morphology were stuck at random orientations on the sides of the plate-like crystals. After numerous screening attempts of small single crystals (<15 μm), we finally managed to isolate and perform a full sphere data collection of the unknown phase. This compound, β-$Ag_2Te(NbS_2)_3$, crystallizes in the noncentrosymmetric $P\bar{6}m2$ space group, with a = 3.2956(6) Å ($=a_1/(3)^{1/2}$), c = 8.220(2) Å, and V = 77.31(3) $Å^3$. The structures of both α-$Ag_2Te(NbS_2)_3$ and β-$Ag_2Te(NbS_2)_3$ are very similar. However, in α-$Ag_2Te(NbS_2)_3$, a distortion of the Ag atomic coordinates (displaying a large thermal parameter, Tables 4 and 5) is seen, while, in β-$Ag_2Te(NbS_2)_3$, the Ag and Te atoms are positionally disordered over all the atomic sites in the [Ag_2Te] layer, resulting in a smaller cell (Tables 6 and 7). EDS analysis confirmed the presence of all four elements at the expected stoichiometry in the small β-$Ag_2Te(NbS_2)_3$ single crystal. Extensive attempts at isolating a single crystal of β-$Ag_2Te(VS_2)_3$ failed, although PDF data on $Ag_2Te(VS_2)_3$ point to the presence of a β-$Ag_2Te(VS_2)_3$ phase analogous to that found in the Nb system (discussed below).

In the parent 2H-NbS_2 structure, the [MS_2] layers are separated by a van der Waals gap (S−S distance) of 3.12 Å,[41] which increases to ∼5.14 Å in $Ag_2Te(MS_2)_3$. Each Ag and Te atom is bonded above and below to S atoms of the [MS_2] layers in a linear coordination environment. The Ag−S distances in both structures are ∼2.53 Å, within the range of a covalent bonding interaction (i.e., a Ag^+ ion bonded to a S^{2-} ion). The Te−S distances in both compounds are roughly ∼2.61 Å; the sum of atomic radii for a Te−S bond is ∼2.4 Å, while typical Te−Te covalent bonds (found in elemental Te) are in the range of ∼2.85 Å; the ionic radius of Te^{2-} is 2.21 Å, while that of S^{2-} is 1.84 Å.[42] The Te−S separation therefore suggests that there is a covalent bond between the two atoms. Moreover, the linear Te coordination environment indicates that the oxidation state of the Te atom is closer to Te^0, similar to that of the central I atom in the $[I_3]^-$ fragment.[43] Hence, association of the [Ag_2Te] layer with the disulfide [MS_2] layers is likely to be a covalent bonding interaction, rather than an ionic one.

Within the [Ag_2Te] layer, the Ag and Te atoms are hexagonally arranged with Ag−Te distances of 3.1898(3) Å for $Ag_2Te(VS_2)_3$ and 3.2961(3) Å for $Ag_2Te(NbS_2)_3$, much longer than the average Ag−Te bond length of ∼2.8 Å, implying that the Ag and Te atoms are not covalently bonded to one another. Interestingly, in $Ag_2Te(NbS_2)_3$, the S(1)−Ag−S(1) bond angle is 166° which prevents the Ag atom from being in an exactly linear coordination as it is slightly off of the site of 3-fold symmetry—this results in a distortion. Lowering the space group symmetry of the crystal structure to *Amm*2 (α'-$Ag_2Te(VS_2)_3$) during single crystal refinement to more accurately model positional disorder resulting from symmetry operations gives a good structure refinement (Table 1), but the atomic displacement parameters for the Ag atoms in the cell are still high and the disorder of the Ag atoms remains. Moreover, in the orthorhombic *Amm*2 structure refinement, the data show that there is a deviation from linearity, or buckling, of the S−Ag−S and S−Te−S angles, which are 175.079(53)° and 176.167(5)°, respectively. This indicates high mobility of the Ag atoms and suggests that there is an interaction between the Ag and Te atoms in the [Ag_2Te] layers. On the basis of the bonding environment of the intercalated metal atoms and the repeat slab unit of one layer, $Ag_2Te(VS_2)_3$ and $Ag_2Te(NbS_2)_3$ are structurally related to the reported 1S-$MTaS_2$ prototype compounds, such as $PbTaSe_2$, $InTaS_2$, and $SnNbSe_2$.[44]

From the single crystal XRD refinements, no evidence of positional disorder was observed for the atoms in the [MS_2] layer. Therefore, structural distortions are likely to originate

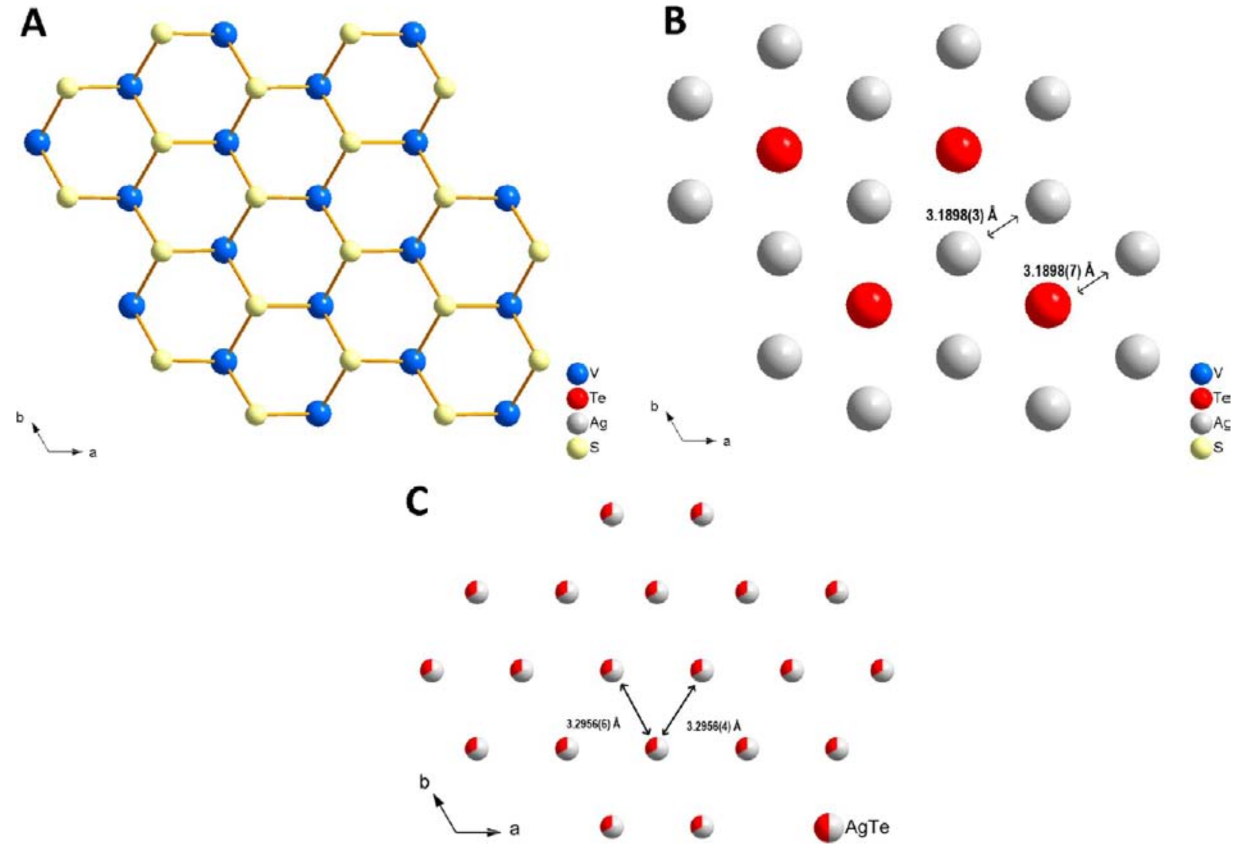

Figure 2. Crystal structure of α-$Ag_2Te(VS_2)_3$: (A) view of the [VS_2] layer down the *c* direction in α-$Ag_2Te(VS_2)_3$; (B) view of the [Ag_2Te] layer down the *c* direction in α-$Ag_2Te(VS_2)_3$; (C) view of the [Ag_2Te] layer down the *c* direction in β-$Ag_2Te(NbS_2)_3$. The colors indicate mixed Ag/Te occupancies over all the atomic positions in the [Ag_2Te] layer.

Table 6. Atomic Coordinates and Equivalent Isotropic Displacement Parameters ($Å^2 \times 10^3$) for β-$Ag_2Te(NbS_2)_3$ at 100(2) K with Estimated Standard Deviations in Parentheses

atom	*x*	*y*	*z*	occupancy	U_{eq}[a]
S	0.0000	0.0000	0.3095(7)	1	2(1)
Nb	0.6667	0.3333	0.5000	1	3(1)
Ag	0.0000	0.0000	0.0000	0.67	33(1)
Te	0.0000	0.0000	0.0000	0.33	33(1)

[a] U_{eq} is defined as one-third of the trace of the orthogonalized U_{ij} tensor.

Table 7. Anisotropic Displacement Parameters ($Å^2 \times 10^3$) for β-$Ag_2Te(NbS_2)_3$ at 100(2) K with Estimated Standard Deviations in Parentheses[a]

atom	U_{11}	U_{22}	U_{33}	U_{12}	U_{13}	U_{23}
S	1(2)	1(2)	5(3)	1(2)	0	0
Nb	2(2)	2(2)	5(2)	1(1)	0	0
Ag	46(2)	46(2)	7(2)	23(1)	0	0
Te	46(2)	46(2)	7(2)	23(1)	0	0

[a] The anisotropic displacement factor exponent takes the form $-2\pi^2[h^2a^{*2}U_{11} + ... + 2hka^*b^*U_{12}]$.

from the intercalated [Ag_2Te] planar layers. In the case of $Ag_2Te(VS_2)_3$, the Ag−Te distance of 3.1898(7) Å is longer than the typical bonding distance, indicating negligible overlap of the Ag and Te orbitals, while the disorder of Ag atoms found in $Ag_2Te(NbS_2)_3$ allows better orbital overlap as a result of closer Ag−Te distances. SAED measurements were performed on single crystals of α-$Ag_2Te(MS_2)_3$ to elucidate the positional disorder that was observed in α-$Ag_2Te(NbS_2)_3$ by the single crystal X-ray diffraction experiment. The electron diffraction patterns are shown in Figure 3, and they are similar for both the α-Nb and α-V members. All the observed reflections were indexed according to the space group $P\bar{6}2m$ that was used for the refinement of the single crystal structures. Neither systematically absent reflections ($P\bar{6}2m$ does not have any extinction conditions) nor additional supercell reflections were observed.

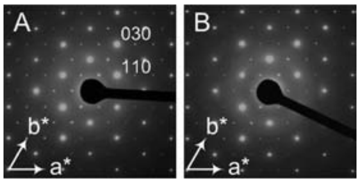

Figure 3. Room temperature selected area electron diffraction viewed along the [001] zone for (A) $Ag_2Te(NbS_2)_3$ and (B) $Ag_2Te(VS_2)_3$. No additional long-range ordering was observed within the hexagonal *ab* plane.

Pair Distribution Function Analyses. The peculiar disorder in $Ag_2Te(NbS_2)_3$ and the lack of any sign of long-range ordering by SAED prompted us to examine its local and long-range structure using the pair distribution function technique (PDF). The advantage of PDF over other crystallographic methods, such as Rietveld and single crystal diffraction analysis, is the elaboration of both Bragg and diffuse intensity

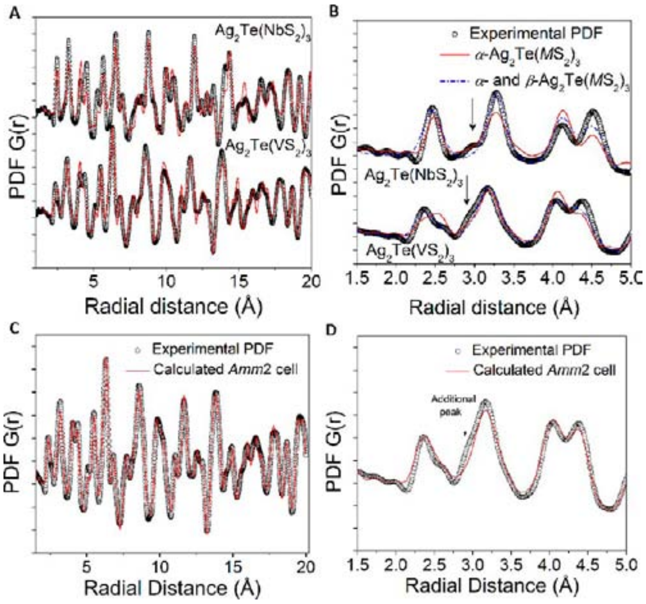

Figure 4. (A) PDF plots for $Ag_2Te(MS_2)_3$. Solid lines represent the fit to the experimental data of the supercell β-$Ag_2Te(MS_2)_3$ model. There is disagreement of the fits in terms of the relative intensity of the peaks. (B) Zoomed in PDF plots for $Ag_2Te(MS_2)_3$ showing the local structure. Solid lines represent the fit to the experimental data of the supercell β-$Ag_2Te(MS_2)_3$ model, and solid-dotted lines represent the fit of the mixture of both α- and β-$Ag_2Te(MS_2)_3$. Although improvement to the fit is significant when using a mixed model, the position and intensity of an additional peak at 2.9 Å in the experimental PDF (shown with arrows) are still not well described. (C) PDF plot of $Ag_2Te(VS_2)_3$ and fit to the *Amm*2 orthorhombic supercell model. A better fit to the relative intensities of the peaks is seen. (D) Zoomed in PDF plot for *Amm*2 fitting of PDF data for $Ag_2Te(VS_2)_3$. The model describes the peak found at 2.9 Å and points to a buckling of the S−Ag−S and S−Te−S angles indicative of interactions between Ag and Te atoms within the $[Ag_2Te]$ layers.

into crystal structure modeling. Thus, as a total scattering technique, PDF can provide information about the local and long-range arrangement of atoms regardless of the degree of ordering. The experimental PDF plots for both $Ag_2Te(NbS_2)_3$ and $Ag_2Te(VS_2)_3$ (Figure 4A) are similar to one another, confirming the isostructural character of the $Ag_2Te(MS_2)_3$ members. The PDF data were fitted against the undistorted ($P\bar{6}2m$) structural model determined by single crystal XRD for α-$Ag_2Te(MS_2)_3$; results are shown with solid lines in Figure 4A. Although the position of the PDF peaks is well described by the models, an apparent disagreement in the relative intensity of the peaks is observed. This was quantified by the agreement factors of 41 and 28% for α-$Ag_2Te(NbS_2)_3$ and α-$Ag_2Te(VS_2)_3$, respectively. Interestingly, in the low *r*-range, where information regarding the local structure can be found, additional peaks in the experimental PDF data at 2.9 Å were observed. These peaks in Figure 4B (shown with arrows) suggest a distorted local environment distinct from the one found crystallographically. Considering the presence of a second polymorph that was found by single crystal XRD, we performed a mixed-phase refinement using both the α- and β-$Ag_2Te(MS_2)_3$ models. The quality of the fits was significantly improved with a much better agreement between the relative intensities of the experimental and calculated PDFs. The overall agreement factors were drastically reduced to 22% (from 41%) and 18% (from 28%) for $Ag_2Te(NbS_2)_3$ and $Ag_2Te(VS_2)_3$, respectively. Nevertheless, although the differences in intensity at the local structure were greatly reduced by the two-phase model (solid-dotted blue line in Figure 4B), the mixed model failed to describe the additional peaks at around 2.9 Å that were observed for both $Ag_2Te(NbS_2)_3$ and $Ag_2Te(VS_2)_3$ (Figure 4B). After testing different models, a lower symmetry *Amm*2 $Ag_2Te(VS_2)_3$ cell was found to describe the experimental PDF data, reinforcing the validity of the single crystal refinement in *Amm*2 (Table 1). The *Amm*2 PDF fitting agreed well with the additional peak at 2.9 Å (Figure 4C,D), with the resulting structural model showing pronounced buckling of the Ag−S (171.93(4)°) and Te−S (178.67(5)°) bond angles. The distance of 2.9 Å may be due to Ag−Ag or Ag−Te contacts, pointing to the presence of significant bonding interactions within the $[Ag_2Te]$ layers for both compounds where in-plane displacement of Ag atoms was observed within the planar layers. In fact, charge transfer could be considered to occur from the Ag atoms to the Te atoms within the $[Ag_2Te]$ layer, while the overlap of the p_z orbitals of the Te atoms could facilitate charge transfer to the $[MS_2]$ layer. This would result in stabilization of the overall structure. Moreover, this suggests that the local structure of both $Ag_2Te(MS_2)_3$ members is distorted, but the structural similarities of both α- and β-forms render the PDF data inconclusive as to which polymorph(s) these distortions belong to.

Thermal Properties. In general, the transition metal dichalcogenides are known to be relatively thermally stable, decomposing at temperatures above 1000 °C. Attempts to melt the compound using an arc melter indicated that the compound decomposes to release S and Te at very high temperatures, both visually and by powder XRD.[20] Temperature-dependent synchrotron powder XRD measurements on the samples were then performed to assess the structural behavior and stability of the title compounds. The data show a decomposition of the $Ag_2Te(VS_2)_3$ structure between 682 and 697 °C into a mixture of binaries which include V_3S_4, VS, and Ag_2Te (Figure 5A). Peaks appearing at 2θ = 8.2, 9.2, and 14.1° at 651 °C correspond to the appearance of VS, while peaks appearing at 2θ = 4.1 and 4.6° at 667 °C correspond to V_3S_4. A peak broadening is seen around 2θ = 6.2° at 667 °C which can be attributed to formation of Ag_2Te. On the other hand, $Ag_2Te(NbS_2)_3$ undergoes a structural rearrangement upon heating between 799 and 814 °C into a structure resembling that of $Na_{0.67}NbS_2$[3a] (Figure 5B). Peaks at 2θ = 6.85, 8.86, and 14.2 °C are seen to gradually increase, while the peak at 17.2° appears with increasing temperature. The disappearance of a peak at 2θ = 5.0° at 760 °C marks the beginning of phase decomposition. Finally, at 814 °C, complete phase conversion is seen (peaks lost with the increase in temperature are marked by red arrows). SEM/EDX performed on a large number of crystals used for the high temperature powder XRD experiment yielded a stoichiometry of $Ag_{0.61}Te_{0.04}NbS_{2.1}$ (±0.06), which indicates that there is evaporation of Te from the structure upon heating of $Ag_2Te(NbS_2)_3$. Therefore, most of the intercalant atoms remaining in the high temperature structure are Ag atoms. In this structure, the NbS_2 layers are staggered relative to one another, and the intercalant atoms lie between the NbS_2 planes, coordinated in trigonal prismatic fashion by S atoms.

The difference in behavior at high temperature between $Ag_2Te(VS_2)_3$ and $Ag_2Te(NbS_2)_3$ may be a result of the greater

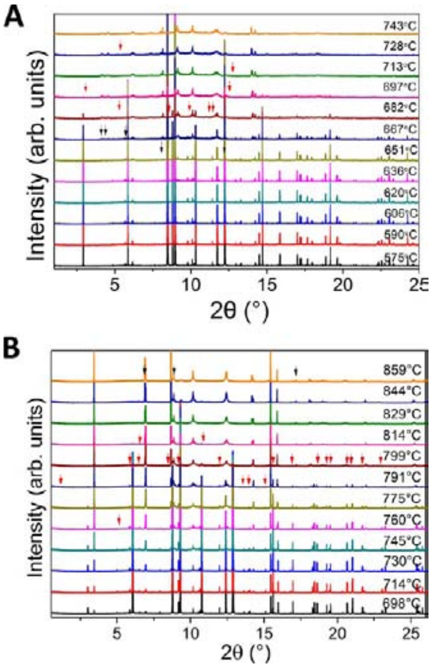

Figure 5. Temperature-dependent powder XRD measurement of (A) $Ag_2Te(VS_2)_3$ and (B) $Ag_2Te(NbS_2)_3$ using a synchrotron radiation source with $\lambda = 0.413$ Å. The appearance of peaks is marked with black arrows, while peaks disappearing are marked with red arrows. In part A, above 682 °C, all peaks above $2\theta = 15°$ have disappeared.

thermal stability of the NbS_2 structure relative to VS_2. That is, the decomposition of the $Ag_2Te(VS_2)_3$ structure to binary compounds V_3S_4 and VS may be because VS_2 itself is not thermally stable. We note that, unlike NbS_2, VS_2 cannot be made directly and is only formed upon chemical deintercalation of $LiVS_2$.[4] Moreover, VS_2 does not form in the 2H polytype (trigonal prismatic coordination of the V atom), which is the coordination environment found in $Ag_2Te(VS_2)_3$. Without structural integrity of the parent dichalcogenide, it is reasonable that the layered structure of $Ag_2Te(VS_2)_3$ cannot stay intact. In contrast, $Ag_2Te(NbS_2)_3$ does not undergo a breakdown of the lamellar NbS_2 substructure but rather rearranges to a different and presumably more stable stacking of the layers.

High-resolution temperature-dependent powder XRD showed no additional impurity phases or signs of decomposition products in the α-$Ag_2Te(VS_2)_3$ samples up to 650 °C (Figure 5A). A Rietveld analysis was performed to assess the presence of β-$Ag_2Te(VS_2)_3$ in the powder samples. The agreement factor of the Rietveld analysis for the a = 5.5247(8), c = 8.022(2) Å α-$Ag_2Te(VS_2)_3$ cell was 10%. Considering the presence of two polymorphs in $Ag_2Te(VS_2)_3$ found by single crystal XRD measurement, a significant improvement in the refinement was achieved when a second hypothetical polymorph (β-$Ag_2Te(VS_2)_3$) with a = 3.2956(6) Å and c = 8.220(2) Å was introduced. The overall agreement factor was reduced to 8%. Since the degree of overlap of the diffraction lines of the (hypothetical) β-$Ag_2Te(MS_2)_3$ phases with those of the α-$Ag_2Te(MS_2)_3$ form is complete (Figure 6A,B), no apparent change in the patterns as a function of temperature was observed. To examine the data more closely, we investigated the change in intensity of the (100) and (101) planes as a function of temperature (Figure 6B,C), but no significant anomalies were observed.

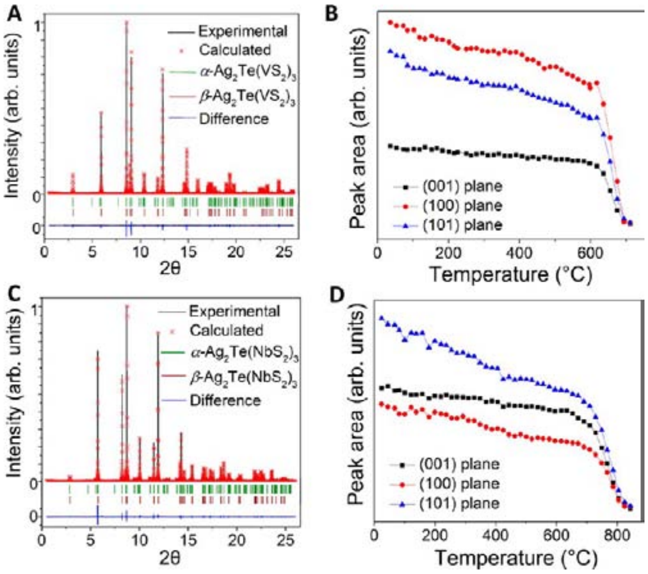

Figure 6. (A) High resolution powder XRD pattern at room temperature for $Ag_2Te(VS_2)_3$ using a synchrotron radiation source with $\lambda = 0.413$ Å. All peaks can be assigned to the proposed models without any impurity phases. There is marked overlap between the polymorphic structures of α-$Ag_2Te(VS_2)_3$ and hypothetical β-$Ag_2Te(VS_2)_3$. The last curve (blue) is the difference between the measured and calculated intensities. (B) Integrated intensity of the powder XRD Bragg reflections of (100) and (101) of $Ag_2Te(VS_2)_3$ as a function of temperature. (C) High resolution powder XRD pattern at 500 °C for $Ag_2Te(NbS_2)_3$. All peaks can be assigned to the proposed models without any impurity phases. The overlap of the polymorphic structures of α-$Ag_2Te(NbS_2)_3$ and β-$Ag_2Te(NbS_2)_3$ is apparent. (D) Integrated intensity of the powder XRD Bragg reflections of (100) and (101) of $Ag_2Te(NbS_2)_3$ as a function of temperature.

High temperature powder XRD experiments at the APS were performed by placing powder samples into capillaries placed in front of a high temperature blower. Because of the long length of the capillary relative to the blower diameter, deintercalation of the structure was found to be irreversible, as excess sulfur was able to condense outside of the edges of the heated region. This is also seen in the high temperature powder XRD data (Figure 5A), where the intensity of $Ag_2Te(VS_2)_3$ is seen to drop drastically at 700 °C. This phenomenon was also observed during heating of $Ag_2Te(VS_2)_3$ past its decomposition temperature with one end of the tube outside of the furnace, resulting in the condensation of elemental S and formation of binary materials in the following scheme:

$$Ag_2Te(VS_2)_3 \rightarrow {}^3\!/_8(V_3S_4 + V_5S_8) + Ag_2Te + {}^3\!/_2 S \quad (1)$$

Likewise, heating of $Ag_2Te(NbS_2)_3$ to about 800 °C resulted in the deintercalation of Te and a rearrangement of the layers in the crystal structure, as seen in the high temperature powder XRD patterns (Figure 5B). The partial and complete deintercalation of Te can be visualized in the following scheme:

$$2Ag_2Te(NbS_2)_3 \rightarrow Ag_2Te_{1-x}(NbS_2)_3 + Ag_2(NbS_2)_3 + (1+x)Te \quad (2)$$

Previously, several reports of intercalated TMDCs with linear coordination of transition or post-transition metal intercalant atoms included $SnTaS_2$,[10a,b] $InTaS_2$,[10a] $PbTaS_2$,[10a] and $AuVS_2$.[10c] These compounds possess interesting temperature-

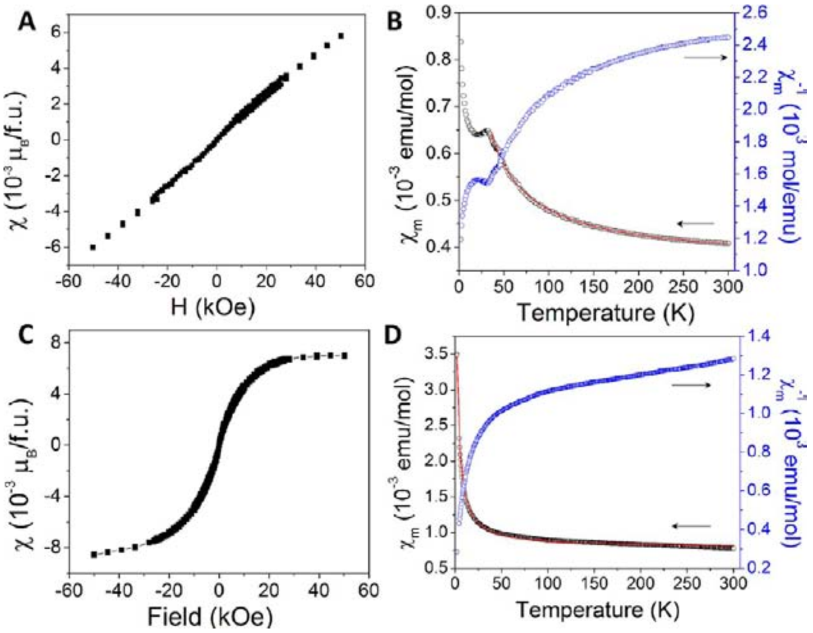

Figure 7. (A) Field-dependent magnetic susceptibility of $Ag_2Te(VS_2)_3$ at 2 K. (B) Zero-field-cooled temperature-dependent magnetic susceptibility of $Ag_2Te(VS_2)_3$. The solid red line indicates the curve of modified Curie−Weiss fit. (C) Field-dependent magnetic susceptibility of $Ag_2Te(NbS_2)_3$ at 2 K. (D) Zero-field-cooled temperature-dependent magnetic susceptibility of $Ag_2Te(NbS_2)_3$. The solid red line indicates the curve of modified Curie−Weiss fit.

dependent properties such as magnetic ordering and superconductivity that are different from the parent compounds TaS_2 and VS_2.[4,10a,45] In $PbTaS_2$ and $SnTaS_2$, an increase in superconducting T_c relative to TaS_2 was thought to be a result of increased electrical conduction from intercalant atom p orbital electrons in intercalant layers.[46] A minimal amount of conduction within the planar $[Ag_2Te]$ layers in $Ag_2Te(MS_2)_3$ would then be expected to suppress the superconducting T_c relative to the parent compounds ($T_c = 6.3$ K in the case of NbS_2). This is also supported by the band structure calculations and DOS where only a small fraction of Ag and Te states cross the Fermi level (Figure 9). In fact, this is reflected in the lack of superconducting transitions in the $Ag_2Te(MS_2)_3$ compounds above 2 K.

Magnetic Properties. The nonlinear magnetic susceptibility behaviors of the $Ag_2Te(MS_2)_3$ compounds were fitted using a modified Curie−Weiss formula to give reasonable values of θ and μ_{eff}. $Ag_2Te(VS_2)_3$ exhibits an increase in magnetization with increasing field at 2 K (Figure 7A). In the analysis of magnetization as a function of temperature, $Ag_2Te(VS_2)_3$ displays an antiferromagnetic−paramagnetic ordering below a Néel temperature of 36 K (Figure 7B). Above this temperature, the paramagnetic region of the curve (36 K to room temperature) shows a fit (agreement factor $R^2 = 99.97\%$) to the modified Curie−Weiss law, with $C = 12.00(1) \times 10^{-3}$ emu·K/mol, $\Theta = -10.0(3)$ K, $\chi_0 = 3.622(3) \times 10^{-4}$ emu/mol, and $\mu_{eff} = 0.179$ μ_B/V atom. The close overlap of the field-cooled and zero-field-cooled temperature-dependent magnetic susceptibility plots of $Ag_2Te(VS_2)_3$ excludes the possibility of spin glass behavior. Deviation from linearity between 50 and 100 K likely arises from a small polarization of any delocalized electrons. The magnetic susceptibility behavior of $Ag_2Te(VS_2)_3$ is very similar to that of V_5S_8, an itinerant antiferromagnet.[47] However, high-resolution powder XRD verified the absence of V_5S_8 as an impurity phase. In V_5S_8, an antiferromagnetic to paramagnetic transition occurs at around 30 K and a low μ_{eff} of ∼1.03 μ_B/V was found to be considerably lower than the calculated spin-only value of 1.73 μ_B for V^{4+} (or the experimentally found μ_{eff} ∼2.64 μ_B[47a]). This was attributed to the presence of both localized and itinerant d electrons contributed by two different types of magnetic V atoms in the structure. In the case of $Ag_2Te(VS_2)_3$, a low μ_{eff} of 0.179 μ_B/V likewise indicates a departure from expected magnetic behavior. In contrast to $Ag_2Te(VS_2)_3$, the magnetization of $Ag_2Te(NbS_2)_3$ saturates around an applied field value of 25 kOe at 2 K (Figure 7C) and displays paramagnetic behavior from 2 to 300 K (Figure 7D). The $Ag_2Te(NbS_2)_3$ magnetic susceptibility curve shows a fit (agreement factor $R^2 = 99.54\%$) to the modified Curie−Weiss law with $C = 9.02(6) \times 10^{-3}$ emu·K/mol, $\theta = -1.37(2)$ K, $\chi_0 = 7.90(1) \times 10^{-4}$ emu/mol, and $\mu_{eff} = 0.155$ μ_B/Nb atom, which is much lower than the calculated spin-only value of 1.73 μ_B for a Nb^{4+} d^1 system. Consistent with our results, literature reports of magnetic studies on group 5 dichalcogenides intercalated with post-transition metals likewise show temperature-independent paramagnetic molar susceptibilities that are lower than that of the pure parent dichalcogenide.[48]

In general, it is thought that post-transition metal intercalation is stabilized by electron transfer from the intercalant p states to the d_{z^2} band metal of the metal, as well as hybridization of intercalant p states with the 3p band of S.[9] This is a possibility for $Ag_2Te(MS_2)_3$ because the Te atoms possess p valence electrons for hybridization, suggesting that there is some oxidation of the metalloid Te atoms and charge transfer from the planar $[Ag_2Te]$ layer to the $[MS_2]$ layer to stabilize the structure. Naturally, the unusual linear coordination of Te atoms in the $[Ag_2Te]$ layer of $Ag_2Te(MS_2)_3$ by S atoms of the sandwiching $[MS_2]$ layers leads to the question of the Te oxidation state. If it is assumed that the planar $[Ag_2Te]$ layer is charge-balanced, then the Te should be found in a 2- oxidation state. Alternatively, because $Ag_2Te(MS_2)_3$ is structurally similar to $SnTaS_2$, the Ag and Te atoms in $Ag_2Te(MS_2)_3$

may possess a charge of 2+ as in $SnTaS_2$. In studying $SnTaS_2$ by photoelectron spectroscopy,[9,49] NMR,[50] and single crystal X-ray diffraction,[10b,51] the oxidation state of the Sn atom was purported to fluctuate between Sn^{2+} and Sn^0. Hence, charge fluctuation of the Ag and/or Te atoms in the intercalant layer may also be a possibility. Still, because the Ag atoms do not have p orbital electrons to contribute to the metal d_{z^2} band, the extent of charge transfer between the $[Ag_2Te]$ and $[MS_2]$ layers in $Ag_2Te(MS_2)_3$ is unlikely to result in oxidation of the Ag atom to 2+ as in the case of the Sn intercalant atoms in $SnTaS_2$. Another possibility seen in the existence of the structurally related compound $AuVS_2$, in which the Au atom has a similar coordination environment to the Ag and Te atoms in $Ag_2Te(MS_2)_3$, suggests that the intercalant layer may carry a 1+ or no charge. Furthermore, the $[S{-}Te{-}S]^{4-}$ structural motif bears a strong resemblance to the triatomic isoelectronic ion I_3^-,[43] where the middle I atom is found in a 1+ oxidation state while the terminal I atoms have formal charges of 1−. This bonding scheme can be rationalized by the model of Rundel, that of a three-center−four-electron (3c−4e) bond. In this 3c−4e model, the valence electrons occupy a σ-bonding molecular orbital and a nonbonding molecular orbital, leaving one empty σ-antibonding molecular orbital.[52] The analogous middle Te in $[S{-}Te{-}S]^{4-}$ would then have a formal charge of 0, while the terminal S atoms would have formal charges of 2−. This type of 3-center, 4-electron bonding is generally only found in T-shaped and square planar Te complexes,[40] rather than in a strictly two-coordinate linear Te environment like that found here. We liken this moiety to the triatomic Se_3^{4-} in $Ba_2Ag_4Se_5$, which the authors conclude is hypervalent and isoelectronic with XeF_2 and I_3^-, containing 22 valence-electron units.[39]

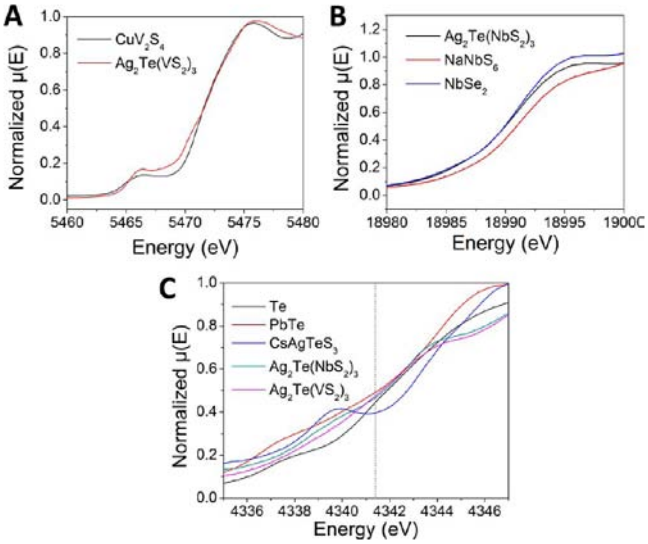

Figure 8. (A) Qualitative analysis of the V XANES K-edge spectra of $Ag_2Te(VS_2)_3$ (black) and CuV_2S_4 (red) showing a close alignment of the absorption edge, with a difference in edge energies of about 1 eV which narrows down the oxidation state of V to be around 3+/4+. (B) Qualitative comparison between the Nb XANES K-edge spectra of $Ag_2Te(NbS_2)_3$ (black), $NaNbS_6$ (Nb^{5+}, red), and $NbSe_2$ (Nb4$^+$, blue) revealing that the Nb absorption edge of $Ag_2Te(NbS_2)_3$ is very closely aligned with that of $NbSe_2$, indicating that the compound features a Nb cation very close to the 4+ oxidation state. (C) A comparison of all the Te XANES L_{III}-edge spectra showing the close proximity of the absorption edges, with $Ag_2Te(VS_2)_3$ (pink) and $Ag_2Te(NbS_2)_3$ (green) very closely aligned and PbTe (red) and Te (black) on either side of the curves in terms of energy. These data are indicative of a Te atom in the $Ag_2Te(MS_2)_3$ compounds that is between Te^0 and Te^{2-}.

XANES Studies. To investigate the extent of electron transfer and intercalant atom valence states in $Ag_2Te(MS_2)_3$, we performed XANES measurements focusing on V, Nb, and Te. Qualitative analysis of the V XANES spectra of $Ag_2Te(VS_2)_3$ and CuV_2S_4 show close alignment of the absorption edges of the two compounds, with a difference in edge energies of about 1 eV (Figure 8A). CuV_2S_4 has been calculated to have mixed V oxidation states of 3+/4+ as a result of atomic orbital hybridization and order−disorder transitions,[28,53] which serves a purpose here of narrowing down the range of possible oxidation states, with the assumption that both of the $Ag_2Te(MS_2)_3$ compounds contain the group V transition metal in the same oxidation state. Qualitative comparison between the Nb XANES spectra of $Ag_2Te(NbS_2)_3$, $NaNbS_6$ (Nb^{5+}), and $NbSe_2$ (Nb^{4+}) reveals that the Nb absorption edge of $Ag_2Te(NbS_2)_3$ is very closely aligned with that of $NbSe_2$ (Figure 8B). This indicates that the compound features a Nb cation very close to the 4+ oxidation state, and implies that the charge transfer of the $[Ag_2Te]$ layer is too small to substantially change the oxidation state of the Nb in the putative parent NbS_2 compound. This is also seen in calculations on $SnTaS_2$ and $LiTaS_2$, where the charge transferred from the intercalant atom does not change the charge on Ta but is rather thought to promote more ionic bonding between the group V metal and the S atom.[54]

In the Te XANES spectra, the absorption edges are all very close in energy (Figure 8C). The elemental Te sample, used as a Te^0 standard, displays a very characteristic pre-edge peak with a local maximum in the derivative peak found at ~4337 eV.[55] The $CsAgTeS_3$, in comparison, exhibits a pre-edge peak as well as a band edge energy shifted to a higher energy of ~4340 eV—both are indicative of a higher Te oxidation state. The dip after the pre-edge peak is also characteristic of a 4+ oxidation state seen in several Te-containing minerals.[55] A comparison of all the Te XANES spectra shows close proximity of the absorption edges, with $Ag_2Te(VS_2)_3$ and $Ag_2Te(NbS_2)_3$ very closely aligned and PbTe and Te on either side of the curves in terms of energy. These data are indicative of a Te atom in the $Ag_2Te(MS_2)_3$ compounds that is between Te^0 and that of Te^{2-}. The results of the XANES analysis prompted further examination of the band structure of the compounds using density functional theory (DFT) calculations.

Calculations and Electronic Transport Properties. Band structure calculations were employed to examine the electronic structure of the $Ag_2Te(MS_2)_3$ (Figure 9). The compounds have similar electronic structures with a valence band maximum just above the Fermi energy, indicating a semimetallic material; this was also verified by the transport measurements. Both the valence and conduction bands in $Ag_2Te(MS_2)_3$ show dispersive character, suggesting high electron and hole mobility. From the density of states (DOS) plots (Figure 9), the valence and conduction bands are mainly composed of transition metal d-states in both compounds with the V-states contributing more than the Nb-states near the Fermi level. The chalcogen p-states and Ag d-states are distributed almost evenly just above and below the Fermi level.

The Seebeck coefficients (Figure 10) and in-plane electrical resistivity values (Figure 11) of single crystal platelets of α-$Ag_2Te(MS_2)_3$ were measured as a function of temperature in an arbitrary direction. The electrical resistivity at room temperature was around 12 $\mu\Omega\cdot$cm for α-$Ag_2Te(VS_2)_3$ and around 11

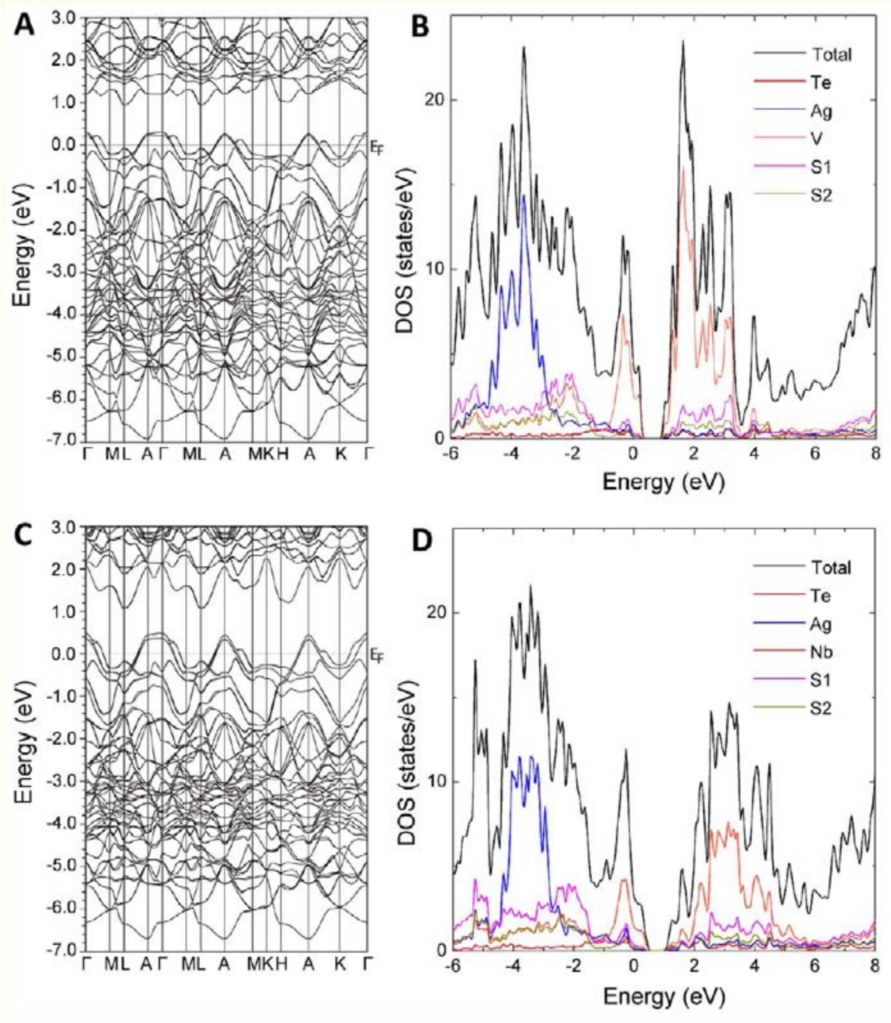

Figure 9. Band structure calculations of $Ag_2Te(MS_2)_3$. Calculated (A) band structure of (B) density-of-states (DOS) plots of $Ag_2Te(VS_2)_3$; calculated (C) band structure of (D) DOS plots of $Ag_2Te(NbS_2)_3$. The compounds have similar electronic structures with a valence band maximum just above the Fermi energy, indicative of semimetals. Both the valence and conduction bands in $Ag_2Te(MS_2)_3$ are disperse, correlating with high electron and hole mobility. From the DOS plots, the valence and conduction bands are mainly composed of transition metal d-states. However, the V-states are seen more than the Nb-states near the Fermi level. The chalcogen p-states and Ag d-states are distributed almost evenly just above and below the Fermi level.

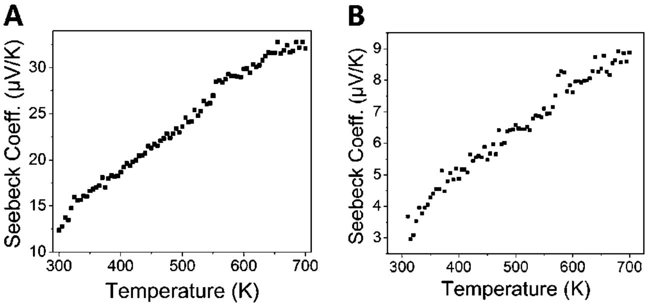

Figure 10. (A) Temperature-dependent Seebeck measurement of (A) $Ag_2Te(VS_2)_3$ and (B) $Ag_2Te(NbS_2)_3$ single crystals from room temperature up to 700 K. The positive sign of the Seebeck values indicates that both materials contain p-type carriers (holes) as the predominant conduction mechanism.

$\mu\Omega\cdot$cm for α-$Ag_2Te(NbS_2)_3$, increasing with temperature which is consistent with the semimetallic behavior suggested by the band structure calculation. These measured values are much lower than the metallic parent dichalcogenide NbS_2[56] and the related $AuVS_2$,[10c] which have room temperature resistivity values of ≥100 $\mu\Omega\cdot$cm; Ag_2Te has a room temperature resistivity of 275 $\mu\Omega\cdot$cm.[57] $SnTaS_2$, a structurally related compound with a metallic intercalant Sn atom, shows resistivity values in the same range as $Ag_2Te(MS_2)_3$.[9] These factors suggest that the Ag and Te atoms within the VS_2 and NbS_2 layers in these compounds are uncharged, resulting in an increase in conductivity of the composite structure relative to the parent dichalcogenides. Moreover, this supports the XANES finding that the small extent of charge transfer between the layers is not enough to substantially change the band structure or the oxidation states of the atoms in the parent dichalcogenide compounds.

The Seebeck coefficient rises with temperature and has a small positive value characteristic of a p-type metal, consistent with the DFT calculations. The room temperature values were around 4 and 2 μV/K for pressed pellet mixtures of α- and β-$Ag_2Te(VS_2)_3$ and α- and β-$Ag_2Te(NbS_2)_3$, respectively. The p-type character was also corroborated by band structure calculations (discussed above). It is expected that, in the

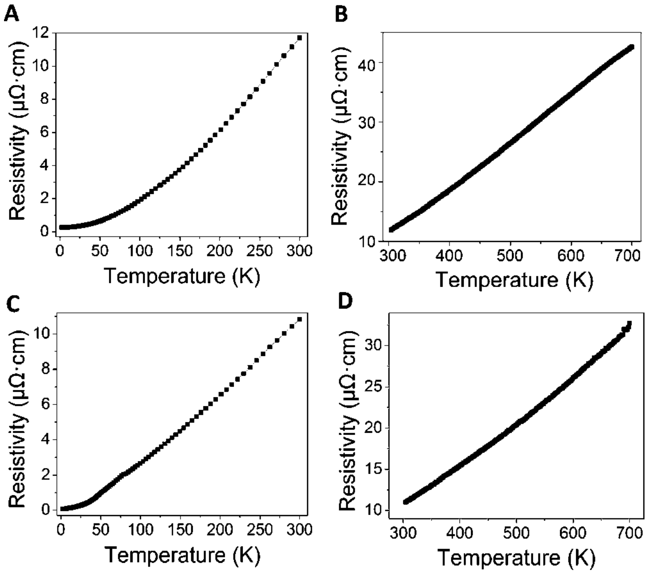

Figure 11. Temperature-dependent resistivity measurement of $Ag_2Te(VS_2)_3$ single crystal from (A) room temperature down to 5 K and (B) up to 700 K; (C) temperature-dependent resistivity measurement of $Ag_2Te(NbS_2)_3$ single crystal down to 5 K and (D) up to 700 K. The resistivity values of these materials increase with increasing temperature, consistent with the behavior of semimetallic materials. The room temperature conductivity values were 12 $\mu\Omega$·cm for α-$Ag_2Te(VS_2)_3$ and around 11 $\mu\Omega$·cm for α-$Ag_2Te(NbS_2)_3$.

group V dichalcogenides, the half-filled conduction band should result in p-type conductivity with the free carriers being holes.[58]

CONCLUSION

New intercalated dichalcogenide compounds, $Ag_2Te(VS_2)_3$ and $Ag_2Te(NbS_2)_3$, are composed of intergrown lattices of $[MS_2]$ and planar $[Ag_2Te]$, where M = V and Nb. Within the structure, the Ag and Te atoms are linearly coordinated by S atoms. Characterization by single crystal XRD revealed the presence of distortions in the $[Ag_2Te]$ layer with a formation of two polymorphs depending on the ordering of the Ag/Te atoms. When the Ag/Te atoms are occupationally disordered, the β-$Ag_2Te(MS_2)_3$ phase is formed. Long-range ordering of Ag and Te atoms in the planar $[Ag_2Te]$ layer yielded a $(3)^{1/2} \times (3)^{1/2}$ supercell and the formation of the α-$Ag_2Te(MS_2)_3$ form. Additionally, PDF analysis uncovered local distortions in the $[Ag_2Te]$ layer resulting from positional displacement of the Ag atoms. These findings support the presence of interactions between the Ag and Te intercalant atoms within the $[Ag_2Te]$ layers that serve to stabilize the linear coordination of the Te atoms, even though the interatomic distances in the ordered models are longer than those of expected bonding interactions. *In-situ* temperature-dependent studies on $Ag_2Te(MS_2)_3$ show a breakdown of the composite structure at elevated temperatures, with either deintercalation or rearrangement which is likely related to the stability of the respective parent dichalcogenide. Considering the makeup of the component layers, $[Ag_2Te]$ and $[MS_2]$, both stable on their own, it is notable that the composite structures are stable to temperatures of ~680 °C.

$Ag_2Te(VS_2)_3$ possesses magnetic properties reminiscent of an itinerant antiferromagnet, V_5S_8, at low temperatures, transitioning to paramagnetism at higher temperatures. The magnetic moments of the V and N atoms in the structure are much lower than expected for d^1 systems, which may be related to the itinerant nature of the electrons. Interestingly, upon insertion of the Ag_2Te layers, the superconductivity of the parent NbS_2 compound at 6.5 K is suppressed down to at least 2 K. The high metallic conductivity of the compounds suggests that the extent of charge transfer is weak and that the filling of the empty d_{z^2} band of the parent dichalcogenide compounds is minimal. However, charge transfer from the $[Ag_2Te]$ layers to the $[MS_2]$ layers and from Ag atoms to Te atoms within the $[Ag_2Te]$ layers is likely to stabilize the unique coordination environment of the Te atoms. Moreover, the X-ray absorption spectra of the compounds indicate the presence of a Te oxidation state that is very close to Te^0. The unique linear coordination environment of Te in a 3-center, 4-electron bond found in $Ag_2Te(MS_2)_3$ contributes to the structural diversity of long-studied Te-containing and dichalcogenide compounds. The hexagonal array of atoms in the Ag_2Te part is a novel arrangement for silver telluride. The stabilization of (Ag_2Te)-(MS_2) adds a new type of intercalated motif to the class of TMDCs after the M'_xMS_2 and the misfit $(M'S)_{1+x}(MS_2)$ compounds. This is a new insight pointing to a variety of intergrowth compounds with metastable arrangements of guest species stabilized between the MS_2 layers.

ASSOCIATED CONTENT

Ⓢ Supporting Information

X-ray crystallographic files (in CIF format) as well as tables for structural information. This material is available free of charge via the Internet at http://pubs.acs.org.

AUTHOR INFORMATION

Corresponding Author

*E-mail: m-kanatzidis@northwestern.edu.

Notes

The authors declare no competing financial interest.

ACKNOWLEDGMENTS

This research was supported by the National Science Foundation grant DMR-1104965. The authors would like to thank Dr. Mahali Balisubramanian (Argonne National Laboratory) and Michael Mara (Northwestern University) for their assistance with XANES experiments and data interpretation and Drs. Jung-Hwan Song and Hosub Jin for band structure discussions. SEM and EDS analyses were performed at the EPIC facility of the NUANCE Center at Northwestern University, supported by NSF-NSEC, NSF-MRSEC, Keck Foundation, the State of Illinois, and Northwestern University. Use of the Advanced Photon Source, an Office of Science User Facility operated for the U.S. Department of Energy (DOE) Office of Science by Argonne National Laboratory, was supported by the U.S. DOE under Contract No. DE-AC02-06CH11357.

REFERENCES

(1) Wilson, J. A.; Yoffe, A. D. *Adv. Phys.* **1969**, *18*, 193.

(2) (a) Wilson, J. A.; Di Salvo, F. J.; Mahajan, S. *Phys. Rev. Lett.* **1974**, *32*, 882. (b) Wilson, J. A.; Salvo, F. J. D.; Mahajan, S. *Adv. Phys.* **1975**, *24*, 117. (c) Moncton, D. E.; Axe, J. D.; DiSalvo, F. J. *Phys. Rev. B: Condens. Matter Mater. Phys.* **1977**, *16*, 801. (d) Fisher, W. G.; Sienko, M. J. *Inorg. Chem.* **1980**, *19*, 39.

(3) (a) Omloo, W. P. F. A. M.; Jellinek, F. *J. Less-Common Met.* **1970**, *20*, 121. (b) Huisman, R.; de Jonge, R.; Haas, C.; Jellinek, F. *J. Solid State Chem.* **1971**, *3*, 56.

(4) (a) Murphy, D. W.; Di Salvo, F. J.; Carides, J. N. *J. Solid State Chem.* **1979**, *29*, 339. (b) Heising, J.; Kanatzidis, M. G. *J. Am. Chem. Soc.* **1999**, *121*, 638. (c) Bissessur, R.; Kanatzidis, M. G.; Schindler, J. L.; Kannewurf, C. R. *Source: Chem. Commun.* **1993**, 1582.

(5) Van Maaren, M. H.; Schaeffer, G. M. *Phys. Lett.* **1966**, *20*, 131.

(6) Van Maaren, M. H.; Schaeffer, G. M. *Phys. Lett. A* **1967**, *24*, 645.

(7) (a) Karnezos, N.; Welsh, L. B.; Shafer, M. W. *Phys. Rev. B: Condens. Matter Mater. Phys.* **1975**, *11*, 1808. (b) *Intercalated Layered Materials*; Levy, F., Ed.; D. Reidel Publishing Company: Dordrecht, Holland, 1979; Vol. *6*.

(8) Liang, W. Y. *Mater. Sci. Eng., B* **1989**, *3*, 139.

(9) Dijkstra, J.; Broekhuizen, E. A.; van Bruggen, C. F.; Haas, C.; de Groot, R. A.; van der Meulen, H. P. *Phys. Rev. B: Condens. Matter Mater. Phys.* **1989**, *40*, 12111.

(10) (a) Di Salvo, F. J.; Hull, J. G. W.; Schwartz, L. H.; Voorhoeve, J. M.; Waszczak, J. V. *J. Chem. Phys.* **1973**, *59*, 1922. (b) Eppinga, R.; Wiegers, G. A. *Mater. Res. Bull.* **1977**, *12*, 1057. (c) Gauzzi, A.; Gilioli, E.; Licci, F.; Marezio, M.; Calestani, G.; Franchini, C.; Massidda, S. *Phys. Rev. B: Condens. Matter Mater. Phys.* **2002**, *66*, 085106.

(11) Wiegers, G. A.; Meetsma, A.; Haange, R. J.; de Boer, J. L. *Mater. Res. Bull.* **1988**, *23*, 1551.

(12) Klemm, W.; Sodomann, H.; Langmesser, P. *Z. Anorg. Allg. Chem.* **1939**, *241*, 281.

(13) See the Supporting Information

(14) Zhang, X.; Kanatzidis, M. G. *J. Am. Chem. Soc.* **1994**, *116*, 1890.

(15) Bensch, W.; Duerichen, P. *Chem. Ber.* **1996**, *129*, 1207.

(16) *X-AREA*; STOE & Cie GmbH, IPDS Software: Darmstadt, Germany, 2006.

(17) *Bruker APEX2*, version 2.1-4 Data Collection, and *SAINT*, version 7.23A; Bruker Analytical X-Ray Instruments, Inc.: Madison, WI, 2007.

(18) Sheldrick, G. M. *Acta Crystallogr., Sect. A: Found. Crystallogr.* **2008**, *64*, 112.

(19) Sheldrick, G. M. *SADABS*; 2008.

(20) Sheldrick, G. M. *SHELXTL*, version 6.14; Bruker Analytical X-Ray Instruments, Inc.: Madison, WI, 2003.

(21) Chupas, P. J.; Qiu, X. Y.; Hanson, J. C.; Lee, P. L.; Grey, C. P.; Billinge, S. J. L. *J. Appl. Crystallogr.* **2003**, *36*, 1342.

(22) Hammersley, A. P.; Svensson, S. O.; Hanfland, M.; Fitch, A. N.; Hausermann, D. *High Pressure Res.* **1996**, *14*, 235.

(23) Egami, T.; Billinge, S. J. L. *Underneath the Bragg Peaks: Structural Analysis of Complex Materials*; Pergamon Press, Elsevier: Oxford, England, 2003.

(24) Qiu, X.; Thompson, J. W.; Billinge, S. J. L. *J. Appl. Crystallogr.* **2004**, *37*, 678.

(25) Farrow, C. L.; Juhas, P.; Liu, J. W.; Bryndin, D.; Bozin, E. S.; Bloch, J. P. T.; Billinge, S. J. L. *J. Phys.: Condens. Matter* **2007**, *19*, 335219.

(26) Kraft, S.; Stumpel, J.; Becker, P.; Kuetgens, U. *Rev. Sci. Instrum.* **1996**, *67*, 681.

(27) Bearden, J. A.; Burr, A. F. *Rev. Mod. Phys.* **1967**, *39*, 125.

(28) Lu, Z. W.; Klein, B. M.; Kurmaev, E. Z.; Cherkashenko, V. M.; Galakhov, V. R.; Shamin, S. N.; Yarmoshenko, Y. M.; Trofimova, V. A.; Uhlenbrock, S.; Neumann, M.; Furubayashi, T.; Hagino, T.; Nagata, S. *Phys. Rev. B: Condens. Matter Mater. Phys.* **1996**, *53*, 9626.

(29) Bensch, W.; Näther, C.; Dürichen, P. *Angew. Chem., Int. Ed.* **1998**, *37*, 133.

(30) (a) Ravel, B.; Newville, M. *J. Synchrotron Radiat.* **2005**, *12*, 537. (b) Newville, M. *J. Synchrotron Radiat.* **2001**, *8*, 322.

(31) Singh, D. *Planewaves, Pseudopotentials, and the LAPW Method*; Kluwer Academic: Boston, MA, 1994.

(32) (a) Kohn, W.; Sham, L. J. *Phys. Rev.* **1965**, *140*, 1133. (b) Hohenberg, P.; Kohn, W. *Phys. Rev. B: Condens. Matter Mater. Phys.* **1964**, *136*, B864.

(33) Perdew, J. P.; Burke, K.; Ernzerhof, M. *Phys. Rev. Lett.* **1996**, *77*, 3865.

(34) Koelling, D. D.; Harmon, B. N. *J. Phys. C: Solid State Phys.* **1977**, *10*, 3107.

(35) Blaha, P.; Schwarz, K.; Madsen, G.; Kvasnicka, D.; Luitz, J.; Schwarz, K. *WIEN2k*; Tech. Univ.: Wien, Vienna, 2001.

(36) (a) Böttcher, P.; Kretschmann, U. *J. Less-Common Met.* **1983**, *95*, 81. (b) Böttcher, P.; Keller, R. *J. Less-Common Met.* **1985**, *109*, 311. (c) Sheldrick, W. S.; Wachhold, M. *Angew. Chem., Int. Ed.* **1995**, *34*, 450. (d) Liu, Q.; Goldberg, N.; Hoffmann, R. *Chem.—Eur. J.* **1996**, *2*, 390.

(37) (a) Dung, N.-H.; Pardo, M.-P.; Boy, P. *Acta Crystallogr., Sect. C: Cryst. Struct. Commun.* **1983**, *39*, 668. (b) Kanatzidis, M. G. *Angew. Chem., Int. Ed.* **1995**, *34*, 2109. (c) Cody, J. A.; Ibers, J. A. *Inorg. Chem.* **1995**, *34*, 3165. (d) Cody, J. A.; Ibers, J. A. *Inorg. Chem.* **1996**, *35*, 3836. (e) Tougait, O.; Daoudi, A.; Potel, M.; Noël, H. *Mater. Res. Bull.* **1997**, *32*, 1239. (f) Wu, E. J.; Pell, M. A.; Ibers, J. A. *J. Alloys Compd.* **1997**, *255*, 106. (g) Narducci, A. A.; Ibers, J. A. *Inorg. Chem.* **1998**, *37*, 3798. (h) Huang, F. Q.; Brazis, P.; Kannewurf, C. R.; Ibers, J. A. *J. Am. Chem. Soc.* **2000**, *122*, 80. (i) Huang, F. Q.; Ibers, J. A. *J. Solid State Chem.* **2001**, *159*, 186. (j) Assoud, A.; Derakhshan, S.; Soheilnia, N.; Kleinke, H. *Chem. Mater.* **2004**, *16*, 4193. (k) Kim, J.-Y.; Gray, D. L.; Ibers, J. A. *Acta Crystallogr., Sect. E: Struct. Rep. Online* **2006**, *62*, i124.

(38) Piers, W. E.; Ferguson, G.; Gallagher, J. F. *Inorg. Chem.* **1994**, *33*, 3784.

(39) Assoud, A.; Xu, J.; Kleinke, H. *Inorg. Chem.* **2007**, *46*, 9906.

(40) (a) Foss, O. *Pure Appl. Chem.* **1970**, *24*, 31. (b) Chung, D.-Y.; Huang, S.-P.; Kim, K.-W.; Kanatzidis, M. G. *Inorg. Chem.* **1995**, *34*, 4292. (c) Hillier, A. C.; Liu, S.-Y.; Sella, A.; Elsegood, M. R. J. *Angew. Chem., Int. Ed.* **1999**, *38*, 2745. (d) Rudd, M. D.; Pahl, D. L.; Hofkens, C. J.; Feazell, R. P. *Phosphorus, Sulfur Silicon Relat. Elem.* **2006**, *181*, 2023. (e) Hrib, C. G.; Jeske, J.; Jones, P. G.; du Mont, W.-W. *Dalton Trans.* **2007**, 3483.

(41) Jellinek, F.; Brauer, G.; Muller, H. *Nature* **1960**, *185*, 376.

(42) Shannon, R. *Acta Crystallogr., Sect. A: Found. Crystallogr.* **1976**, *32*, 751.

(43) (a) Pimentel, G. C. *J. Chem. Phys.* **1951**, *19*, 446. (b) Munzarová, M. L.; Hoffmann, R. *J. Am. Chem. Soc.* **2002**, *124*, 4787. (c) Otsuka, M.; Mori, H.; Kikuchi, H.; Takano, K. *Comput. Theor. Chem.* **2011**, *973*, 69.

(44) Eppinga, R.; Wiegers, G. A. *Physica B+C* **1980**, *99*, 121.

(45) Myron, H. W. *Physica B+C* **1980**, *99*, 243.

(46) Guo, G. Y.; Liang, W. Y. *J. Phys. C: Solid State Physics* **1987**, *20*, 4315.

(47) (a) De Vries, A. B.; Haas, C. *J. Phys. Chem. Solids* **1973**, *34*, 651. (b) Nozaki, H.; Umehara, M.; Ishizawa, Y.; Saeki, M.; Mizoguchi, T.; Nakahira, M. *J. Phys. Chem. Solids* **1978**, *39*, 851. (c) Forsyth, J. B.; et al. *J. Phys. C: Solid State Phys.* **1979**, *12*, 4261.

(48) Rao, G. V. S.; Schafer, M. W. In *Intercalated Layered Materials*; Levy, F., Ed.; D. Reidel Publishing Company: Dordrecht, Holland, 1979; Vol. *6*, p 99.

(49) Eppinga, R.; et al. *J. Phys. C: Solid State Phys.* **1976**, *9*, 3371.

(50) Gossard, A. C.; Salvo, F. J. d.; Yasuoka, H. *Phys. Rev. B: Condens. Matter Mater. Phys.* **1974**, *9*, 3965.

(51) van der Lee, A.; Wiegers, G. A. *Mater. Res. Bull.* **1990**, *25*, 1011.

(52) Rundle, R. E. *J. Am. Chem. Soc.* **1963**, *85*, 112.

(53) (a) Hidaka, M.; Tokiwa, N.; Wijesundera, R. P.; Awaka, J.; Nagata, S.; Park, Y. J.; Lee, K. B. *Phys. Status Solidi B* **2007**, *244*, 2565. (b) Kumara, L. S. R.; Hidaka, M.; Tokiwa, N.; Awaka, J.; Hagino, T.; Nagata, S.; Park, Y. J. *Phys. Status Solidi B* **2008**, *245*, 2539.

(54) Blaha, P. *J. Phys.: Condens. Matter* **1991**, *3*, 9381.

(55) Grundler, P. V.; Brugger, J.; Meisser, N.; Ansermet, S.; Borg, S.; Etschmann, B.; Testemale, D.; Bolin, T. *Am. Mineral.* **2008**, *93*, 1911.

(56) (a) Naito, M.; Tanaka, S. *J. Phys. Soc. Jpn.* **1982**, *51*, 219. (b) Motizuki, K.; Nishio, Y.; Shirai, M.; Suzuki, N. *Phys. B* **1996**, *219–220*, 83.

(57) Fujikane, M.; Kurosaki, K.; Muta, H.; Yamanaka, S. *J. Alloys Compd.* **2005**, *387*, 297.

(58) Marseglia, E. A. *Int. Rev. Phys. Chem.* **1983**, *3*, 177.

(59) Cary, D. R.; Ball, G. E.; Arnold, J. *J. Am. Chem. Soc.* **1995**, *117*, 3492.